*Article*

# Mesh-Based 3D MEC Modeling of a Novel Hybrid Claw Pole Generator

**Yu Cao** *[iD], **Chuang Liu and Junyue Yu**

College of Automation Engineering, Ming Palace Campus, Nanjing University of Aeronautics and Astronautics, Nanjing 211106, China; lc@nuaa.edu.cn (C.L.); yjy@nuaa.edu.cn (J.Y.)
*   Correspondence: yu_cao_bx1403516@nuaa.edu.cn; Tel.: +86-138-0517-1667

**Abstract:** A brushless parallel hybrid excitation claw pole generator (HECPG) is proposed for electric vehicle (EV) application. Permanent magnet (PM) excitation method can reduce the volume of the machine and improve the power density and efficiency. Moreover, the voltage regulation can be ensured by field excitation. The flux path of the proposed HECPG is complex, and it will take a long time for 3D finite element analysis (FEA) to process it. To reduce simulation time, the mathematical model of the generator is given by a mesh-based 3D magnet equivalent circuit (MEC) network method considering radial and axial flux, magnetic saturation, and magnetic flux leakage. The performance of the generator is analyzed by FEA and prototype experiment. Finally, the results of 3D MEC, FEA, and experiment are compared. There is little difference between the three results, so 3D MEC can ensure the accuracy and significantly reduce the simulation time. The efficiency of the proposed HECPG is 90%, and the DC-Bus voltage can be modulated by changing the amplitude of field current.

**Keywords:** claw pole generator (CPG); hybrid excitation (HE); magnet equivalent circuit (MEC); permanent magnet (PM)

---

## 1. Introduction

The claw pole machine was widely applied in electric vehicle (EV) applications. A typical claw pole generator (CPG) consists of a conventional stator that is equipped with a multiphase overlapping or nonoverlapping winding, and the two sets of claw pole rotors are nested together. Conventional claw pole machine's drawbacks lie in the following four aspects: (1) slip ring system is used; (2) low efficiency; (3) low power density; (4) high claw-to-claw leakage. Although permanent magnet (PM) excitation can improve the power density and efficiency of the generator, the extensive use of PM leads to the high cost of claw pole machine and the voltage cannot be modulated, thus the requirements in EV application cannot be met [1–4]. The voltage regulation can be ensured by field excitation. By changing the amplitude of field current, the voltage can be adjusted. In this paper, a brushless parallel hybrid excitation claw pole generator (HECPG) is proposed. PM excitation and field excitation are combined to increase the power density and efficiency. Moreover, the ability to adjust voltage is realized. Some typical structures that were reported are as follows.

Chenfeng and Yang proposed a hybrid excitation synchronous machine with an asymmetrically staggered permanent magnet [5]. A special inner stator was designed to locate the ring-shaped field winding. Open-circuit magnetic flux adjustment range reached +60%/−60%, and torque control range reached 55%. Y. Kuroda proposed a parallel hybrid excitation motor in which the coil magnetic field winding and the ferrite magnet were located on the rotor [6]. The efficiency was improved by using parallel hybrid flux path. A. Ibala proposed the axial auxiliary excitation motor structure [7,8]. This structure was beneficial to the design of excitation windings and the optimization of internal space layout. K. L. Kovalev proposed a brushless superconducting synchronous generator with

claw-shaped poles and PM [9]. The excitation current was controlled to modulate the output voltage of the generator. Although generator losses were greatly reduced due to superconductivity, it was difficult to meet the requirements in EV system. G. Dajaku proposed a hybrid excitation machine with two kinds of rotors [10]. Two additional axial rotor components were added to increase the air-gap flux density under the machine active length. The additional PM rotors boost the air-gap rotor flux. A new brushless electrically excited claw-pole generator for vehicle power generation was proposed, and it can reach about 92% conversion efficiency within 7.2 kW power scale [11]. A hybrid excited claw pole electric machine was proposed, and the hybrid excitation was performed with a conventional coil located between two parts of the claw-shape rotor and additional permanent magnets, which are placed on claw poles. The efficiency of the machine can reach about 81% [12].

It was proved in the above research works that the power density and efficiency can be improved by using parallel hybrid excitation method, and the voltage can be adjusted by field excitation. However, the structure of CPG is complicated, and the hybrid magnetic flux path is 3D. It is time-consuming to carry out 3D finite element analysis (FEA). Magnetic equivalent circuit (MEC) method was used for decades as a tool for machine analysis. MEC methods enable one to model any machine with an extremely small number of elements, retaining a very high computational accuracy. A 3D MEC model of Lundell machines was built in [13–18]. H. W. Derbas et al. compared the Nodal- and mesh-based MEC models [19]. This proved that a mesh formulation can yield a model that is much more efficient numerically than that of the nodal MEC method. M. L. Bach developed a mesh-based MEC for the time-varying function [20]. An iteration algorithm was presented with a criterion to engage for converging at arbitrary levels. Also, it seems more likely that for a mesh-based MEC, a relaxation setting during iteration could be unnecessary. D. Elloumi et al. proposed a 3D MEC model for hybrid-excited CPG, which was incorporated into the rotor motion [21,22]. Different flux tubes between stators and rotors were revealed. Newton–Raphson iteration is set up to derivate flux linkage and back EMF. R. Rabhi et al. emphasized leakage flux and the saturation effect inside CPG [23]. Leakage fluxes between claw poles are also taken into account. The authors proposed a new type of hybrid excitation generator and used the 3D MEC method to establish an equivalent model of the generator [24]. A prototype test platform was established to verify that the EMC method had a higher calculation accuracy and a much shorter calculation time.

In this paper, a brushless parallel hybrid excitation claw pole generator (HECPG) is proposed, based on taking the pros and cons of the above papers into account. First, the structure and working principle of the proposed HECPG are introduced. Then, the mathematical model of the proposed HECPG is derived based on 3D MEC. Finally, the performance of the proposed HECPG is analyzed by FEA and prototype experiment. The results of 3D MEC, FEA, and experiment are compared to prove the effectiveness of 3D MEC, and higher power density, higher efficiency, and regulated voltage can be obtained through hybrid excitation.

## 2. Generator Structure and Working Principle

### 2.1. Generator Structure

The proposed HECPG is based on a claw pole rotor structure, in which two sets of claw pole rotors are nested together to increase machine power density and efficiency [6,7,10]. The exploded view of the proposed HECPG is shown in Figure 1. PMs are inserted in the interpolar region and also on the outer circle, so that each claw pole finger is enclosed by three pieces of PM: one radially, and the other two tangentially, as shown in Figure 2b. The DC excitation coils are located on both sides of the ending cover, which is brushless.
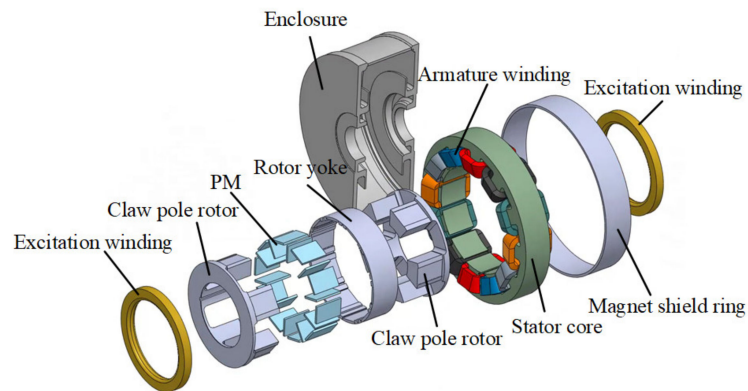
**Figure 1.** Exploded view of hybrid excitation claw pole generator (HECPG).
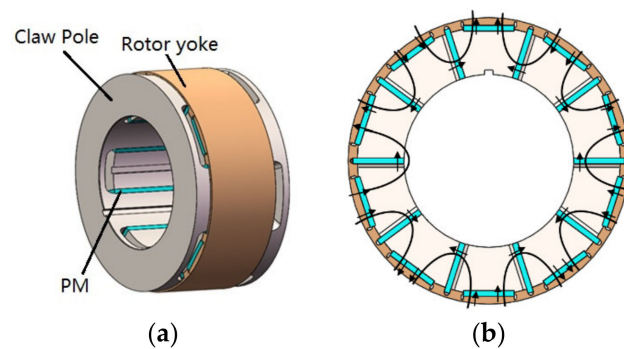


**Figure 2.** Rotor layout: (**a**) overview; (**b**) cross-section.

Two sets of three-phase armature winding, where one set lags 30 electric degrees behind the other, are connected to double three-phase diode rectifier circuit to supply the DC-Bus; thus, current ripple can be reduced, and harmonic factor is optimized. The slot star diagram of armature winding is shown in Figure 3a, and its winding connection layout is shown in Figure 3b. The schematic diagram of rectifier circuit is shown in Figure 3c.
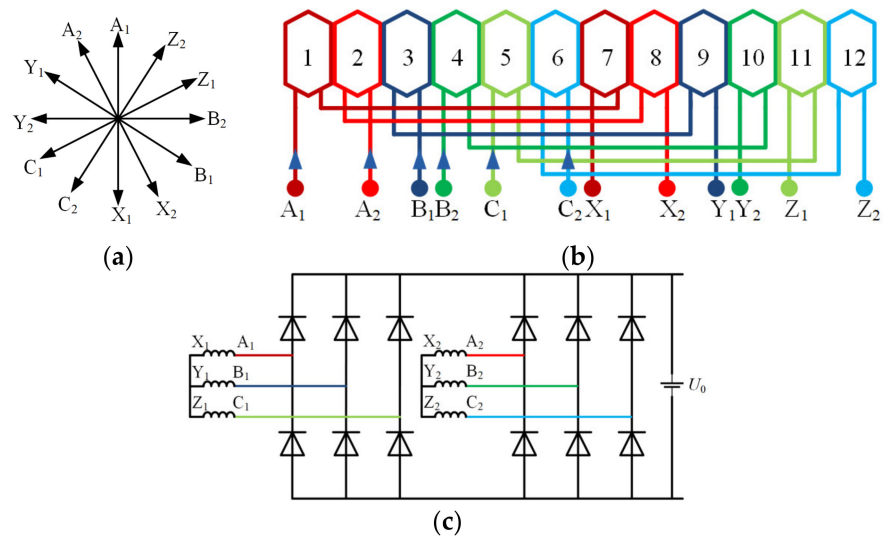


**Figure 3.** Armature winding and circuit diagram: (**a**) slot star diagram of armature winding; (**b**) armature winding connection layout; (**c**) schematic diagram of rectifier circuit.

Because of advantages such as short end-winding, high slot filling factor, low cogging torque, greater tolerance, and low manufacturing costs, a 12-slot, 10-pole fractional slot-concentrated winding is chosen as the armature layout, as shown in Figure 3b. Benefits

are obtained with this armature layout, the fundamental harmonic winding factor is improved, and many harmonics in main air gap flux are eliminated. The dual three-phase winding topology combines the advantages of single layer for higher winding factor and the advantages of double layer winding for low MMF harmonic contents. The spatial layout of the dual three-phase stator winding is shown in Figure 4.
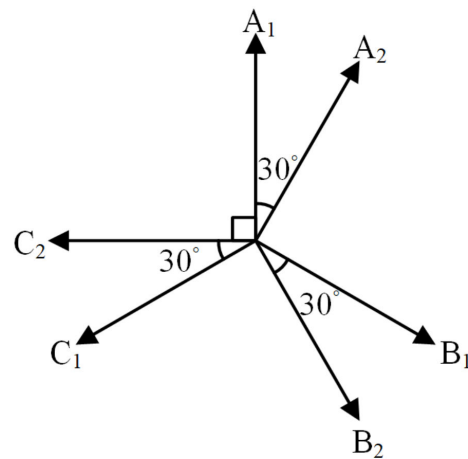


**Figure 4.** Spatial layout of dual three-phase stator winding.

### 2.2. Working Principle

The hybrid flux path in HECPG is shown in Figure 5. The magnetic flux distribution in HECPG by FEA is shown in Figure 6. Figure 6a corresponds to Figure 5a, and Figure 6b corresponds to Figure 5c. The magnetic flux distribution results of FEA can verify the correctness of the hybrid flux path.



(a)

(b)

(c)

(d)
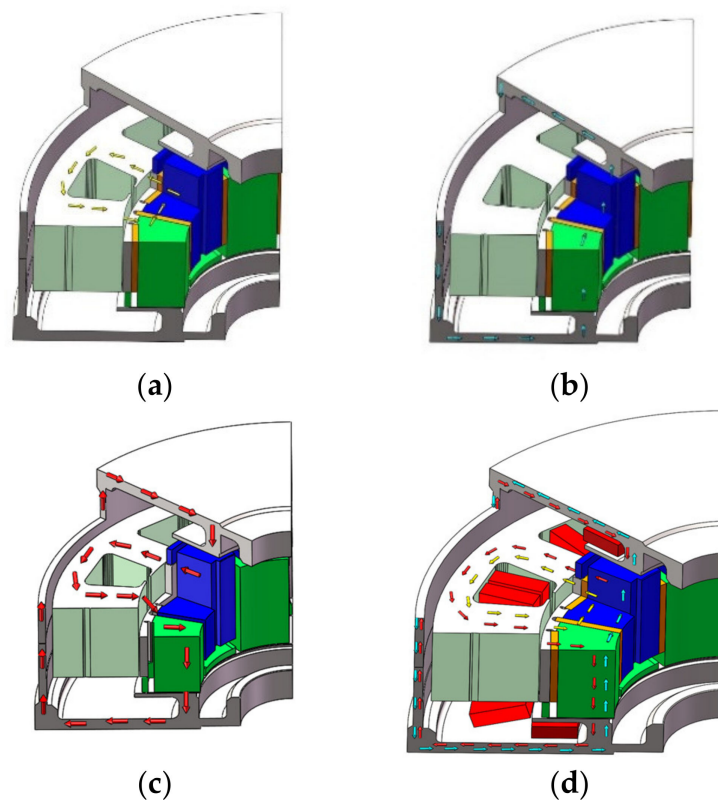
**Figure 5.** Hybrid flux path in HECPG: (**a**) first permanent magnet (PM) flux path; (**b**) second PM flux path; (**c**) field excitation flux path; (**d**) hybrid flux path.

(**a**)           (**b**)
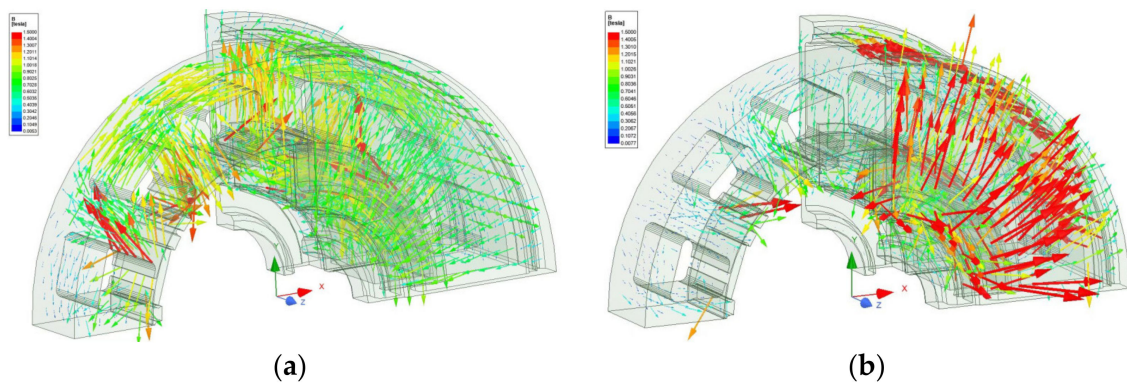
**Figure 6.** Magnetic flux distribution in HECPG by finite element analysis (FEA): (**a**) PM only; (**b**) field excitation only.

The hybrid flux path is as follows:

(1) First PM flux path is the main flux path, which is shown by yellow arrows in Figure 5a. The specific path is: Rotor claw pole finger (the blue one)-radial PM-rotor yoke-main air gap-stator tooth-stator yoke-adjacent stator tooth-main air gap-rotor yoke-radial PM-rotor claw pole finger (the green one)-tangential PM-rotor claw pole finger (the blue one).

(2) Second PM flux path is the magnetic flux leakage path, which is shown by blue arrows in Figure 5b. The specific path is: Rotor claw pole finger (the blue one)-claw pole endplate-upper axial air gap-upper magnet bridge-upper ending cover-enclosure-lower ending cover-lower magnet bridge- lower axial air gap-claw pole endplate-rotor claw pole finger (the green one)-tangential PM-rotor claw pole finger (the blue one).

(3) Field excitation flux path, which is shown by red arrows in Figure 5c. The specific path is: Upper DC coil-upper magnet bridge-upper axial air gap-rotor claw endplate-claw pole finger (the blue one)-radial PM-rotor yoke-main air gap-stator tooth-stator yoke-adjacent stator tooth-main air gap-rotor yoke-radial PM-rotor claw pole finger (the green one)-rotor claw endplate-axial air gap-lower magnet bridge-lower DC coil-lower ending cover-enclosure-upper ending cover-upper DC coil.

These three flux paths constitute the hybrid flux path, as shown in Figure 5d. When the amplitude of field current is increased in positive direction, the magnetic flux increases, and the back EMF and DC-Bus voltage increase because the field excitation flux path and first PM flux path are in the same direction. When the amplitude of field current is increased in negative direction, the magnetic flux decreases, and the back EMF and DC-Bus voltage decrease because the field excitation flux path and first PM flux path are in the opposite direction. Therefore, the voltage can be modulated by changing the direction and amplitude of field current.

## 3. Design Optimization

### 3.1. Calculation of Reluctance

To obtain a reluctance network of HECPG, the rotor yoke surface is discretized into three nodes for each median plane claw, and armature magnetic reaction and air gap reluctance for the rotor motion are taken into account. By neglecting magnetic saturation, reluctance can be calculated in (1). Thus, the reluctance of the air gap or iron can be derived as a function of $\theta_r$:

$$R(\theta_r) = \frac{L}{\mu \times S} \tag{1}$$

$$R(\theta_r) = \frac{L}{\phi} H\left(\frac{\phi}{S}\right) \tag{2}$$

The division of $\phi$ by the flux tube equivalent surface $S$ yields the flux density $B$. The magnetic field of $H$ is then derived from the *B-H* characteristic of the involved material. Finally, $H$ is multiplied by the ratio of the flux tube length $L$ by $\phi$. Therefore, the iron reluctance could be derived in (2), considering magnetic saturation as a function of $\theta_r$.

The dual three-phase armature currents are shown in (3):

$$
i_{abcs} = \begin{bmatrix} i_{a1} \\ i_{a2} \\ i_{b1} \\ i_{b2} \\ i_{c1} \\ i_{c2} \end{bmatrix} = \sqrt{2}I_s \begin{bmatrix} \cos p\theta_r \\ \cos\left(p\theta_r - \frac{\pi}{6}\right) \\ \cos\left(p\theta_r - \frac{2\pi}{3}\right) \\ \cos\left(p\theta_r - \frac{5\pi}{6}\right) \\ \cos\left(p\theta_r + \frac{2\pi}{3}\right) \\ \cos\left(p\theta_r + \frac{\pi}{2}\right) \end{bmatrix} \tag{3}
$$

### 3.2. Three-Dimensional-MEC Network Topologies

A 3D-MEC network was established in Figures 7 and 8, considering different rotor motions in the machine. Figures 7 and 8 are limited to one half of the complete scheme, so only five poles are shown, and the armature current and PM are both working. Meanwhile, the influence of the toroidal excitation coil is expressed as an MMF source similar to PM. The tangential PM was simplified and considered as the radial PM for convenience. It is apparent the 3D-MEC network in the scope of 0°–180° mechanical angle is identical to that of 180°–360°. The leakage flux tube and axial flux tube are drawn in red lines in Figures 7 and 8.

Radial flux tubes include $R_{y1}$–$R_{y6}$, $\phi_{ag1}$–$\phi_{ag19}$, $R_{st1}$–$R_{st6}$, $R_{ry1}$–$R_{ry16}$, $R_{rt1}$–$R_{rt5}$, $R_{PM1}$–$R_{PM5}$, $F_{st1}$–$F_{st6}$, $F_{PM1}$–$F_{PM5}$, $\phi_{st1}$–$\phi_{st6}$, $\phi_{ag1}$–$\phi_{ag19}$, and $\phi_{rt1}$–$\phi_{rt5}$. Axial flux tubes include $R_p$, $R_{aa}$, $R_{at1}$–$R_{at5}$, $R_{aa}$, $F_{DE}$, and $\phi_{at1}$–$\phi_{at5}$. Leakage flux tubes include $R_{TL1}$–$R_{TL6}$; $R_{ry}$ refers to discretized leakage reluctance in rotor yoke, as well as $R_{cc}$.

In the meantime, each rotor claw is counter-symmetric from the adjacent one, i.e.,

$$
\phi_{rt1} = -\phi_{rt2} = \phi_{rt3} = -\phi_{rt4} = \phi_{rt5} \tag{4}
$$

In Figure 8, Kirchhoff's law (KVL) can be applied around each loop.

The upper mesh, where $\phi_{rt1}$–$\phi_{rt6}$ flow through, corresponds to a total of six equations, and only $\phi_{rt1}$ is shown in Figure 7. In Figure 8, $\phi_{ag2}$ should be replaced by $\phi_{ag1}$:

$$
\begin{aligned}
&\left(R_{st1} + R_{y1} + R_{st2} + R_{TL1}\right)\phi_{st1} + R_{st1}\phi_{st6} \\
&-R_{TL1}\phi_{ag2} - R_{st2}\phi_{st2} = F_{st1}
\end{aligned} \tag{5}
$$

and

$$
F_{st1} = N_{a1}i_{a1} + N_{a2}i_{a2} \tag{6}
$$

The middle-level mesh network where $\phi_{ag1}$–$\phi_{ag19}$ flow through, corresponds to a total of 19 equations, and only $\phi_{ag1}$ is shown in Figure 7. In Figure 8, $\phi_{rt1}$ should be replaced by $\phi_{rt5}$:

$$
\begin{aligned}
&\left(R_{ag1} + R_{ry1} + R_{ag2} + R_{ry2}\right)\phi_{ag1} \\
&-\left(R_{ag2} + R_{ry2}\right)R_{ag2} \\
&+\left(R_{ag1} + R_{ry1}\right)\phi_{ag19} - R_{ry}\phi_{rt1} = 0
\end{aligned} \tag{7}
$$

The axial excitation mesh network, where $\phi_{at1}$–$\phi_{at5}$ flow through, corresponds to a total of five equations, and only $\phi_{at1}$ is shown in Figures 7 and 8:

$$
\begin{aligned}
&\left(R_{aa} + R_{at1} + R_p + R_{PM1} + R_{rt1}\right)\phi_{at1} \\
&-\left(R_{PM1} + R_{rt1}\right)\left(\phi_{rt1} + \phi_{rt5}\right) = F_{DE} - F_{PM1}
\end{aligned} \tag{8}
$$
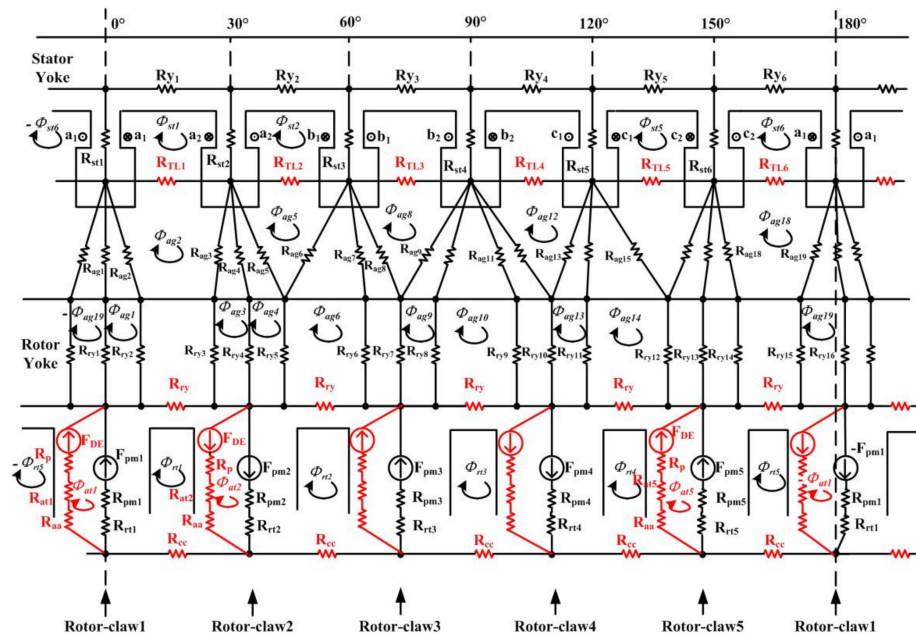
**Figure 7.** Magnet equivalent circuit (MEC) network for HECPG ($\theta_r = 0°$).
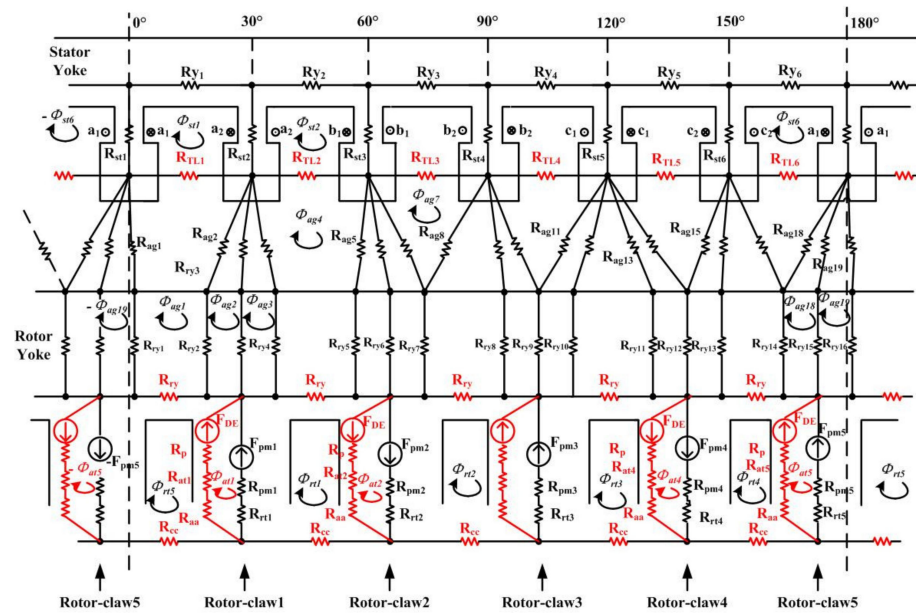


**Figure 8.** MEC network for HECPG ($\theta_r = 35°$).

The bottom-level mesh network, where $\phi_{rt1}$–$\phi_{rt5}$ flow through, due to counter-symmetry of the topology, which is explained above, only $\phi_{rt1}$ is shown in Figure 7. In Figure 8, $\phi_{ag2}$ should be replaced by $\phi_{ag4}$:

$$
\begin{aligned}
&(R_{rt1} + R_{PM1} + R_{ry} + R_{PM2} + R_{rt2} + R_{cc})\phi_{rt1} \\
&-R_{ry}R_{ag2} + (R_{PM1} + R_{rt1})(\phi_{rt5} - \phi_{at1}) \\
&+(R_{PM2} + R_{rt2})(\phi_{at2} - \phi_{rt2}) = F_{PM1} + F_{PM2}
\end{aligned}
\tag{9}
$$

A system of nonlinear algebraic equations can be obtained from (5)–(9):

$$
A_R^{(nlxnl)}\phi_1^{(nlx1)} = F_1^{(nlx1)}
\tag{10}
$$

Each row in (10) represents a KVL equation. The components can be expanded as:

$$\phi_1 = \left[ \begin{array}{ccccccc} \phi_{st1} & \cdots & \phi_{stns} & \phi_{rt1} & \phi_{at1} & \phi_{ag1} & \cdots & \phi_{agna} \end{array} \right]^T \tag{11}$$

where the subscripts *st*, *rt*, *at*, and *ag* indicate loop fluxes in the stator teeth, rotor teeth, axial air gap, and main air gap, respectively. The subscripts *ns* and *na* indicate the number of air gap loops, respectively. Using similar subscripts, $F_1$ is expanded as:

$$F_1 = \left[ \begin{array}{ccccc} F_{st1} & \cdots & F_{stns} & F_{PM1} & F_{DE} & 0^{(1xna)} \end{array} \right]^T \tag{12}$$

In the case of this paper, *ns* = 6, *na* = 19, *nl* = 27. In general, the reluctances within a stator or rotor loop are independent of rotor position, and thus are easily established. However, only the air gap reluctance changes when rotor position changes. The number of air gap loops remains the same.

In general, $A_R$ can be expressed:

$$A_R = \begin{bmatrix} A_{st}^{(nsxns)} & 0 & 0 & A_{ag,st}^{(nsxna)}(\theta_r) \\ 0 & A_{PM} & A_{PM,DE} & A_{ag,PM}^{(1xna)}(\theta_r) \\ 0 & (A_{PM,DE})^T & A_{DE} & A_{ag,DE}^{(1xna)}(\theta_r) \\ A_{ag,st}^T & A_{ag,PM}^T & A_{ag,DE}^T & A_{ag}^{(naxna)}(\theta_r) \end{bmatrix} \tag{13}$$

The submatrices ($A_{ag,st}$, $A_{ag,PM}$, $A_{ag,DE}$, $A_{ag}$) are rotor position-dependent and must be updated for each position. When HECPG is at the initial rotor position $\theta_{r0}$, the flux density is assumed to be zero in the machine. The relative flux tube topology is formed, and two algorithms of reluctance are applied to establish the matrix $A_R$, in which one is the case under saturated magnetic circuit, which is shown in (2). Another is the case under nonsaturated magnetic circuit, e.g., air gap, which is shown in (1).

The complete mesh-based MEC network model is used to calculate the performance of the machine. The flux vector can be solved by the N-R iteration algorithm.

*3.3. Three-Dimensional-MEC Network Solution*

The initial condition ($k$ = 0) can be expressed:

$$\phi^{(1)}(\theta_r) = A_R^{(k)}(\theta_r)F_1(\theta_r) \tag{14}$$

In the case of $k > 0$:

$$\phi^{(k+1)} = \phi^{(k)} - \left( J^{(k)} \right)^{-1} \cdot \left( A_R^{(k)}\phi^{(k)} - F \right) \tag{15}$$

When the difference between the loop flux at iteration $k$ and $k + 1$ is within a user-defined tolerance, the solution for the rotor position is then obtained, as shown in (16). The flowchart of the developed numerical procedure is illustrated in Figure 9:

$$\left\| \phi^{(k+1)} - \phi^{(k)} \right\| \leq \varepsilon \tag{16}$$

When HECPG is at next rotor position $\theta_{r1}$, a new initial loop flux is calculated from (7) using a new initial matrix $A_R^{(k)}(\theta_{r1})$, based on the flux topology of the new position. $A_R$ and $J$ should be updated when HECPG is moved to a new rotor position.

Finally, the back EMF can be expressed:

$$E = \frac{1}{\sqrt{2}} N_a \omega \phi_m \tag{17}$$

The magnetic saturation is considered in the proposed 3D MEC, and the no-load back EMF in a certain position can be predicted. The flux leakage, such as claw finger to endplate, is neglected in this paper. This is one of the reasons why the experimental results deviate from FEA and 3D MEC. In the proposed 3D MEC, the main flux leakage, including flux leakage between stator teeth, rotor teeth, and claws, is taken into account.
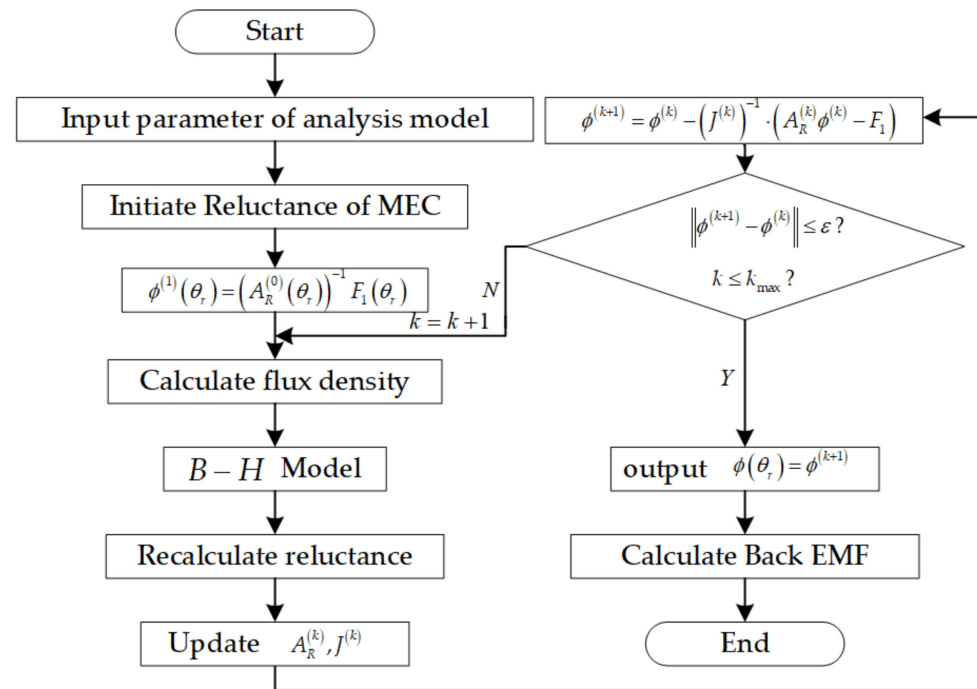


**Figure 9.** Analysis procedure of 3D-MEC.

The parameters of the generator model obtained by initial design are listed in Table 1. They are obtained by considering the design requirements; for example, the output power needs to be 10 kW.

**Table 1.** Parameters of generator model by initial design.

| Parameters | Value |
|---|---|
| Stator outer diameter | 312 mm |
| Stator inner diameter | 200 mm |
| Effective core length | 52 mm |
| Rotor outer diameter | 198.8 mm |
| Rotor inner diameter | 120 mm |
| Rated current | 10 A |
| Winding factor | 0.966 |
| Number of slots | 12 |
| Stacking factor | 0.9 |
| Armature winding turns | 210 |
| Stator yoke width | 17 mm |
| Stator tooth width | 28.28 mm |
| PM (NdFeB 38UH) remanence | 1.22–1.26 T |
| PM (NdFeB 38UH) recoil permeability | 1.05 |
| PM (NdFeB 38UH) coercive force | ≥915 kA/m |
| PM length | 53 mm |

Main air gap length, axial air gap length, PM depth, PM width, and slot width have great influence on machine performance, thus these five parameters are optimized by 3D MEC and FEA. The optimized parameters are listed in Table 2.

**Table 2.** Optimized generator parameters.

| Parameters | Value |
|---|---|
| Main air gap length | 0.6 mm |
| Axial air gap length | 0.7 mm |
| PM depth | 4 mm |
| PM width | 36 mm |
| Slot width | 7 mm |

## 4. Simulation and Experiment

A HECPG prototype is manufactured, and its design parameters are given in Tables 1–3. The prototype structure is shown in Figure 10a–c. The test platform is shown in Figure 10d. The dragging motor is a variable speed AC induction motor. The type of rectifier bridge is VUO 35-18 No.7. An oscilloscope is used to display various waveforms, and its type is TDS3032B. The type of torque sensor is WPL-2. More results about machine performance are obtained by 3D MEC and FEA. The accuracy of 3D MEC is verified by comparing the 3D MEC results, FEA results, and experimental results.

**Table 3.** Prototype parameters.

| Parameters | Value/Type |
|---|---|
| Rated power | 10 kW |
| DC-Bus voltage | 900 V DC |
| Rated speed | 3000 rpm |
| Machine type | Claw-pole |
| Max Weight | 60 kg |
| Pole pitch ratio | 0.78 |
| Number of phases | 3 |
| Rectifier bridge type | VUO 35-18 No.7 |



(a)　　　　　　　　　　(b)　　　　　　　　　　(c)



(d)
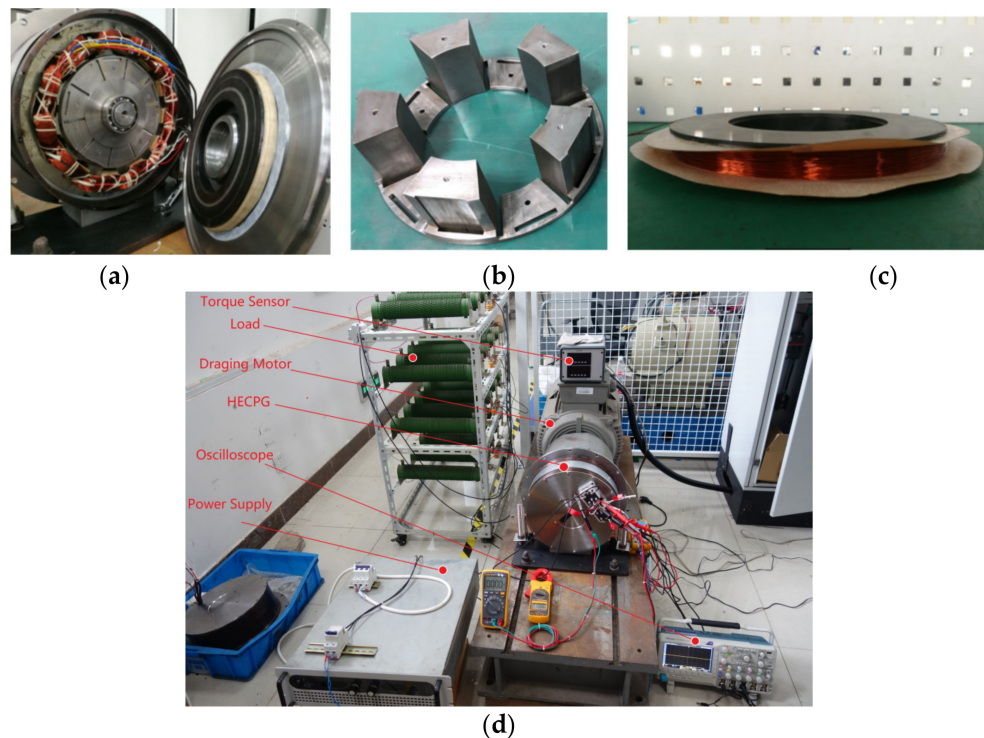
**Figure 10.** Prototype: (**a**) integral structure; (**b**) claw pole rotor; (**c**) axial magnetic bridge; (**d**) test platform.

The distribution of flux density under different excitation currents is shown in Figure 11. Figure 11a shows that flux density in stator is 1.3 T when $i_f = 0$ A. The flux density in stator increases to 1.5 T when $i_f = 4$ A, as shown in Figure 11b. It is proved that the excitation winding can adjust the excitation field effectively.



(a)



(b)
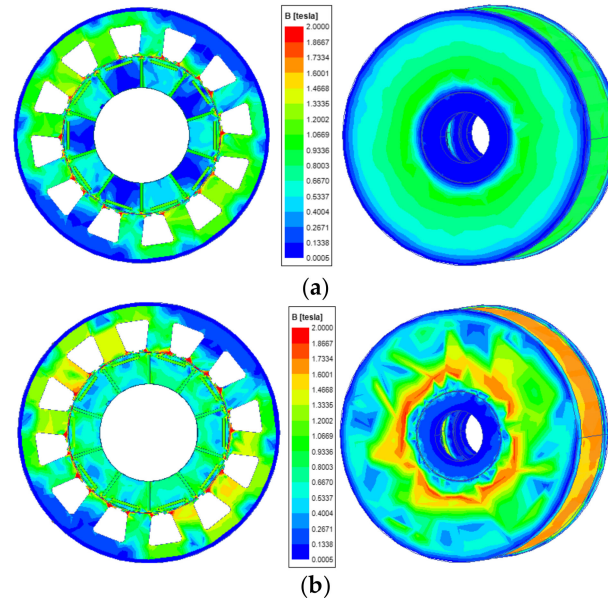
**Figure 11.** Flux density nephogram at no-load condition. (a) $i_f = 0$ A; (b) $i_f = 4$ A.

*4.1. No-Load Characteristics*

The no-load back EMF of A1 and A2 phases is shown in Figure 12. The amplitude of back EMF is about 400 V. The waveforms of FEA and experiment are basically consistent. Comparing Figure 12a to Figure 12b, the FEA results are very close to experimental results. The total harmonic distortion (THD) of A1 phase back EMF in FEA results and experimental results are 25.4% and 25.1%, respectively.



(a)



(b)
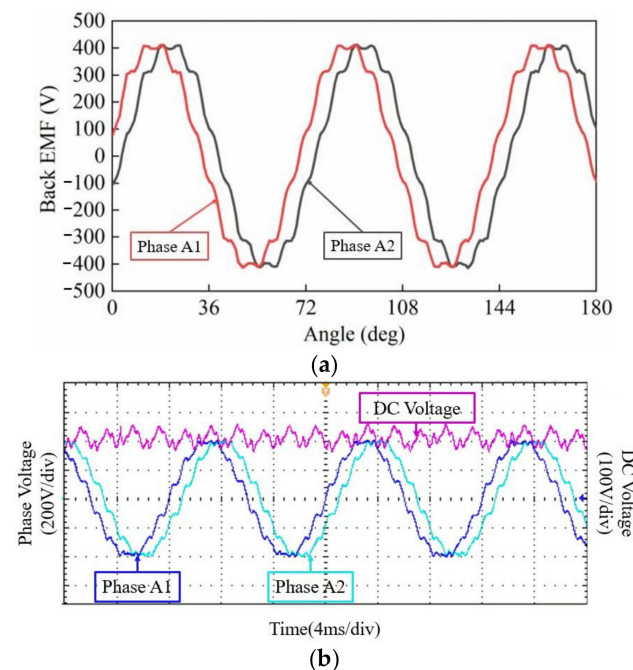
**Figure 12.** Back EMF of A1 and A2 phases. (a) FEA results; (b) experimental results.

In Figure 13, when the field current is 4 A, the no-load DC-Bus voltage is significantly higher than that of 0 A. The no-load DC-Bus voltage can be modulated from 845 V to 1250 V by adjusting field current at the rated rotation speed of 3000 rpm. The DC voltage difference between FEA and 3D MEC is not large. The maximum absolute error of FEA, 3D MEC, and experiment are 122 V, 128 V, 27 V, respectively. The root mean square error of FEA, 3D MEC, and experiment are 1251, 1270, 1181, respectively. It is proved that the 3D MEC method can achieve a high accuracy. The voltage obtained from the experiment is lower than FEA and 3D MEC, because some losses and magnetic leakage are not taken into account in FEA and 3D MEC. It takes 20 h by FEA, while it only costs 4 h by 3D MEC. The 3D MEC method can help reduce the simulation time and speed up the machine design procedure.
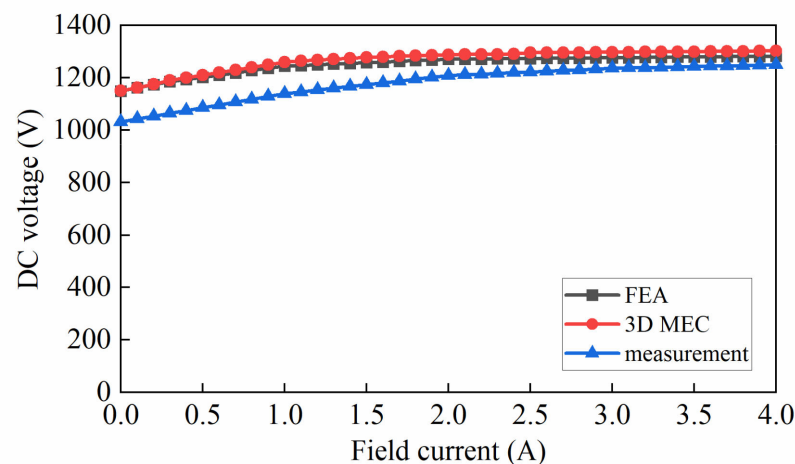


**Figure 13.** DC-Bus voltage.

The relationship between bus voltage and excitation current at different speeds is shown in Figure 14. The bus voltage increases linearly with the increase in speed. It is proved that the output voltage of the generator can be effectively adjusted with the change of speed.
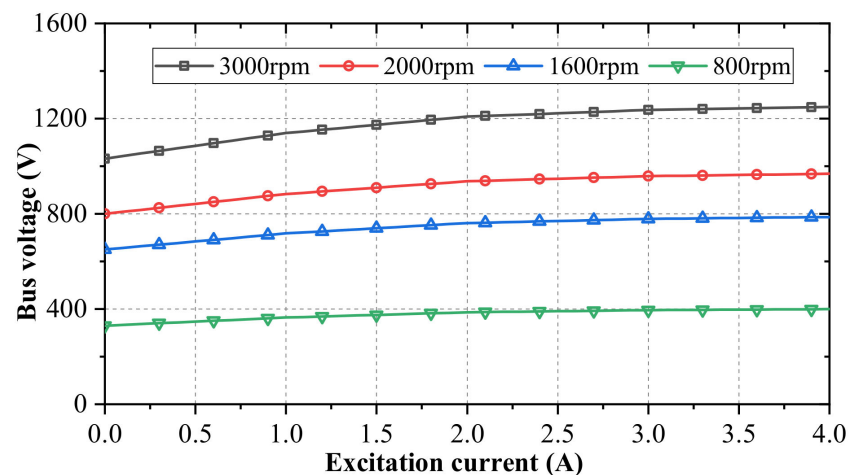


**Figure 14.** No-load voltage at different speeds.

*4.2. Load Characteristics*

As shown in Figure 15, the DC terminal voltage is gradually reduced with the rise of load current; therefore, the field current needs to be constantly adjusted to stabilize the output voltage of the generator. The results of 3D MEC are consistent with those of FEA. The results of the 3D MEC and FEA are in good agreement with the experimental results.
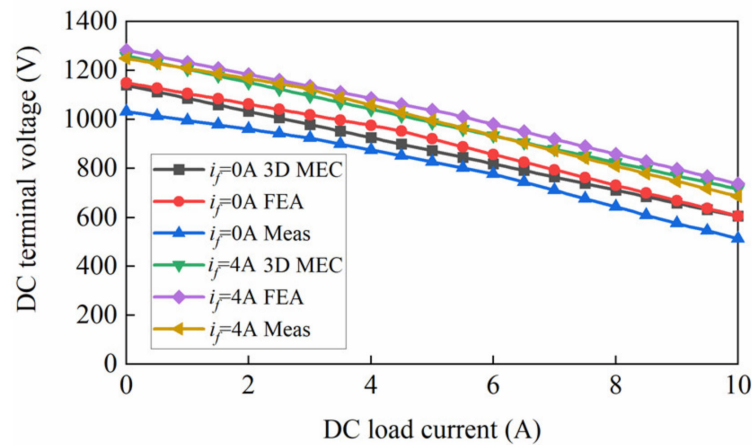
**Figure 15.** External characteristics.

The DC-Bus voltage, which is modulated by field current at full load, varies from 958 V to 1128 V. The full load is set as an 80Ω resistor, thus the output power at the full load can be lifted from 11475 W up to 15907 W, which is a 39% increase in the output power. In the prototype experiment, the output voltage increases from 856 V to 991 V when the excitation current is changed from 0 A to 4 A, which is a 16% increase in the output voltage.

The rated speed of the HECPG is 3000 r/min, and the output voltage is shown in Figure 16. Under the rated load, the average output voltage is 900 V, the output current is 11.36 A, and the output power is 10.28 kW. The proposed HECPG meets the design requirements (output power ≥10 kW).
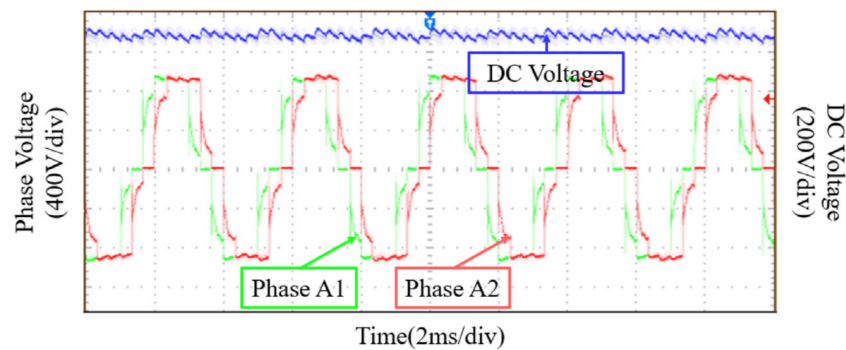


**Figure 16.** External characteristics validation.

In Figure 17, the proposed HECPG achieves a relatively high efficiency, which is acceptable for an EV power supply.
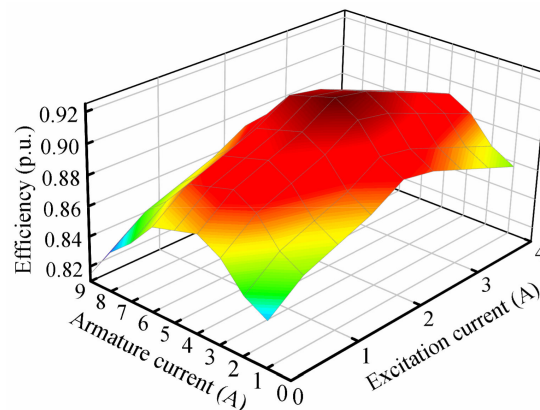


**Figure 17.** Three-dimensional efficiency map.

In general, the machine efficiency is 90% (Including generator and power electronic control module). With the increase in current, the efficiency increases, and then decreases. The main reason is that the copper loss increases significantly when the current increases.

The rated power of the proposed HECPG is 10.28 kW, and its efficiency can reach 90%. The electrically excited claw pole generator reported in [11] can reach about 92% conversion efficiency within 7.2 kW power scale. The hybrid excited claw pole electric machine reported in [12] can reach about 81% efficiency, but its rated power is unknown. The performances comparison is shown in Table 4. The proposed HECPG has higher rated power, and the efficiency is about 90%, slightly lower than that of the machine in [11].

**Table 4.** Performance comparison.

|  | Proposed HECPG | Electrically Excited Claw Pole Generator Reported in [11] | Hybrid Excited Claw Pole Electric Machine Reported in [12] |
|---|---|---|---|
| Rated power | 10.28 kW | 7.2 kW | - |
| Efficiency | 90% | 92% | 81% |

## 5. Conclusions

A brushless parallel hybrid excitation claw pole generator (HECPG) is proposed for electric vehicle (EV) application. The hybrid excitation method can improve the power density and efficiency. Further, the voltage can be modulated by changing the amplitude of field current. The machine structure and working principle are illustrated. To reduce simulation time, the mathematical model of HECPG is given by a mesh-based 3D magnet equivalent circuit (MEC) method considering radial and axial flux, magnetic saturation, and magnetic flux leakage. The results of 3D MEC, finite element analysis (FEA), and experiment are compared. The DC-Bus voltage waveforms in no-load characteristics show that the voltage can be modulated from 845 V to 1250 V by adjusting field current. A good agreement was noticed between the DC-Bus voltage waveforms of 3D MEC and FEA in load characteristics; therefore, 3D MEC can ensure the accuracy and significantly reduce the simulation time. The voltage obtained from the experiment is lower than FEA and 3D MEC, because some losses and magnetic leakage are not taken into account in FEA and 3D MEC. The 3D MEC could help further optimize the important parameters in the generator, such as air gap length, permanent magnet (PM) depth, PM width, and slot width.

A HECPG prototype is manufactured, and its experimental platform is established. The output power and efficiency of the proposed HECPG are 10.28 kW and 90%, respectively. The DC-Bus voltage can be modulated by changing the amplitude of field current. The generator performances prove that the proposed HECPG is a decent power supply for EV application that requires high power density, high efficiency, and wide flux-weakening range.

**Author Contributions:** Y.C. implemented the research, performed the analysis, and wrote the paper; C.L. provided guidance and supervision; J.Y. conceived the idea of the research and implemented experiment on test bench. All authors have read and agreed to the published version of the manuscript.

**Institutional Review Board Statement:** Not applicable.

**Informed Consent Statement:** Not applicable.

**Data Availability Statement:** Not applicable.

**Conflicts of Interest:** The authors declare no conflict of interest.

## Nomenclature

| | |
|---|---|
| $R_{y1}$–$R_{y6}$ | circumferential stator yoke reluctance |
| $\phi_{ag1}$–$\phi_{ag19}$ | different main air-gap flux linkage |
| $R_{st1}$–$R_{st6}$ | each stator tooth radial reluctance |
| $R_{ry1}$–$R_{ry16}$ | each discretized rotor yoke radial reluctance |
| $R_{rt1}$–$R_{rt5}$ | each rotor yoke radial reluctance |
| $R_{PM1}$–$R_{PM5}$ | each claw pole rotor PM reluctance in the radial and tangential direction |
| $F_{st1}$–$F_{st6}$ | each stator tooth mesh MMF caused by armature windings |
| $F_{PM1}$–$F_{PM5}$ | each claw pole rotor PM MMF in the radial and tangential direction |
| $\phi_{st1}$–$\phi_{st6}$ | each stator slot mesh flux linkage |
| $\phi_{ag1}$–$\phi_{ag19}$ | each main air-gap mesh flux linkage |
| $\phi_{rt1}$–$\phi_{rt5}$ | each rotor slot mesh flux linkage |
| $R_p$ | equivalent axial reluctance |
| $R_{aa}$ | equivalent axial air gap reluctance |
| $R_{at1}$–$R_{at5}$ | each claw pole rotor axial reluctance |
| $R_{aa}$ | average axial air gap reluctance |
| $F_{DE}$ | each claw pole rotor mesh equivalent axial excitation MMF |
| $\phi_{at1}$–$\phi_{at5}$ | each claw pole rotor mesh equivalent axial flux linkage |
| $R_{TL1}$–$R_{TL6}$ | leakage reluctance between stator teeth |
| $R_{ry}$ | discretized leakage reluctance in rotor yoke |
| $R_{cc}$ | claw leakage reluctance |
| $L$ | path length |
| $\mu$ | permeability of the material |
| $S$ | sectional area of flux flow |
| $\phi$ | magnetic flux predicted by 3D MEC |
| $\theta_r$ | rotor angle |
| $N_{a1}$, $N_{a2}$ | winding turns of $i_{a1}$, $i_{a2}$, respectively |
| $i_{a1}$, $i_{a2}$ | armature winding a1 current, armature winding a2 current, respectively |
| $A_R$ | symmetric matrix composed of reluctance |
| $\phi_1$ | vector of loop fluxes |
| $F_1$ | vector of MMF sources |
| $nl$ | number of flux loops |
| $A_{st}$, $A_{PM}$ | stator and rotor loops, respectively |
| $A_{DE}$ | axial flux loop |
| $J$ | Jacobian matrix |
| $k$ | iteration step number |
| $Na$ | number of turns of armature windings per phase |
| $\omega$ | angular frequency |
| $\phi_m$ | flux linkage per phase which is predicted by the MEC |
| $i_f$ | field current |

## References

1. Martinez-Munoz, D.; Alakula, M. Comparison between a Novel Claw-Pole Electrically Magnetized Synchronous Machine without Slip-Rings and a Permanent Magnet Machine. In Proceedings of the IEEE International Electric Machines and Drives Conference, IEEE IEMDC, Madison, WI, USA, 1–4 June 2003; IEEE: New York, NY, USA; pp. 1351–1356.
2. Zhang, F.G.; Zhang, S.F.; Bai, H.J.; Nolle, E.; Gruenberger, H.P. Magnetic Field Analysis and Performance Calculation for New Type of Claw Pole Motor with Permanent Magnet Outer Rotor. In Proceedings of the CES/IEEE 5th International Power Electronics and Motion Control Conference, IEEE 5th IPEMCC, Shanghai, China, 14–16 August 2006; pp. 827–831.
3. Liu, X.P.; Lin, H.Y.; Zhu, Z.Q.; Yang, C.; Fang, S.; Guo, J. A Novel Dual-Stator Hybrid Excited Synchronous Wind Generator. *IEEE Trans. Ind. Appl.* **2009**, *45*, 947–953. [CrossRef]
4. Li, L.; Kedous-Lebouc, A.; Foggia, A.; Mipo, J.C. Influence of Magnetic Materials on Claw Pole Machines Behavior. *IEEE Trans. Magn.* **2010**, *46*, 574–577. [CrossRef]
5. Yang, C.F.; Lin, H.Y.; Guo, J.; Zhu, Z.Q. Design and Analysis of a Novel Hybrid Excitation Synchronous Machine with Asymmetrically Stagger Permanent Magnet. *IEEE Trans. Magn.* **2008**, *44*, 4353–4356. [CrossRef]
6. Kuroda, Y.; Morita, M.; Hazeyama, M.; Azuma, M.; Inoue, M. Improvement of a claw pole motor using additional ferrite magnets for hybrid electric vehicles. In Proceedings of the XIX International Conference on Electrical Machines-ICEM 2010, IEEE ICEM, Rome, Italy, 6–8 September 2010.

7.   Ibala, A.; Masmoudi, A. 3D FEA Based Feature Investigation of a Claw Pole Generator with DC Excitation in the Stator. In Proceedings of the 7th Multi-conference on Systems, Signals and Devices, Amman, Jordan, 27–30 June 2010.

8.   Zhang, Z.R.; Ma, S.J.; Dai, J.; Yan, Y.G. Investigation of Hybrid Excitation Synchronous Machines with Axial Auxiliary Air-Gaps and Non-Uniform Air-Gaps. *IEEE Trans. Indu. Appl.* **2014**, *50*, 1729–1737. [CrossRef]

9.   Kovalev, K.L.; Verzhbitsky, L.G.; Kozub, S.S.; Penkin, V.T.; Larionov, A.E.; Modestov, K.A.; Ivanov, N.S.; Tulinova, E.E.; Dubensky, A.A. Brushless Superconducting Synchronous Generator with Claw-Shaped Poles and Permanent Magnets. *IEEE Trans. Appl. Supercond.* **2016**, *26*, 1–4. [CrossRef]

10.   Dajaku, G.; Lehner, B.; Dajaku, X.; Pretzer, A.; Gerling, D. Hybrid Excited Claw Pole Rotor for High Power Density Automotive Generators. In Proceedings of the 2016 XXII International Conference on Electrical Machines (ICEM), IEEE XXII ICEM, Lausanne, Switzerland, 4–7 September 2016; IEEE: New York, NY, USA; pp. 2536–2543.

11.   Zhao, X.; Niu, S.; Ching, T.W. Design and Analysis of a New Brushless Electrically Excited Claw-Pole Generator for Hybrid Electric Vehicle. *IEEE Trans. Magn.* **2018**, *54*, 1–5. [CrossRef]

12.   Wardach, M. Hybrid excited claw pole electric machine. In Proceedings of the 2016 21st International Conference on Methods and Models in Automation and Robotics (MMAR), Miedzyzdroje, Poland, 29 August–1 September 2016; IEEE: New York, NY, USA; pp. 152–156.

13.   Hecquet, M.; Brochet, P. Time variation of Forces in a Synchronous Machine Using Electric Coupled Network Model. *IEEE Trans. Magn.* **1998**, *34*, 3214–3217. [CrossRef]

14.   Ostovic, V.; Miller, J.M.; Garg, V.K.; Schultz, R.D.; Swales, S.H. A Magnetic-Equivalent-Circuit-Based Performance Computation of a Lundell Generator. *IEEE Trans. Indu. Appl.* **1999**, *35*, 825–830. [CrossRef]

15.   Bai, H.; Pekarek, S.D.; Tichenor, J.; Eversman, W.; Buening, D.J.; Holbrook, G.R.; Krefta, R.J. Incorporating the Effects of Magnetic Saturation in a Coupled-Circuit Model of a Claw-Pole Generator. *IEEE Trans. Ener. Conv.* **2007**, *22*, 290–298. [CrossRef]

16.   Liu, Y.; Zhang, Z.R.; Dai, J. Feature Investigation of Axial Flux Leakage of a Hybrid Excitation Synchronous Machine. In Proceedings of the 2014 17th International Conference on Electrical Machines and Systems (ICEMS), IEEE 17th ICEMS, Hangzhou, China, 22–25 October 2014; IEEE: New York, NY, USA; pp. 1971–1976.

17.   Hecquet, M.; Brochet, P. Modeling of a Claw-Pole generator Using Permeance Network Coupled with Electric Circuits. *IEEE Trans. Magn.* **1995**, *31*, 2131–2134. [CrossRef]

18.   Ibala, A.; Masmoudi, A. Accounting for the Armature Magnetic Reaction and Saturation Effects in the Reluctance Model of a New Concept of Claw-Pole Generator. *IEEE Trans. Magn.* **2010**, *46*, 3955–3961. [CrossRef]

19.   Derbas, H.W.; Williams, J.M.; Koenig, A.C.; Pekarek, S.D. A Comparison of Nodal—And Mesh-Based Magnetic Equivalent Circuit Models. *IEEE Trans. Ener. Conv.* **2009**, *24*, 388–396. [CrossRef]

20.   Bash, M.L.; Williams, J.M.; Pekarek, S.D. Incorporating Motion in Mesh-Based Magnetic Equivalent Circuits. *IEEE Trans. Ener. Conv.* **2010**, *25*, 329–338. [CrossRef]

21.   Elloumi, D.; Ibala, A.; Rebhi, R.; Masmoudi, A. 3D MEC Modeling of a Hybrid-Excited Claw Pole Generator Incorporating the Rotor Motion. In Proceedings of the International Conference on Sustainable Mobility Applications, Renewables and Technology (SMART), Kuwait, Kuwait, 23–25 November 2015.

22.   Elloumi, D.; Ibala, A.; Rebhi, R.; Masmoudi, A. Lumped Circuit Accounting for the Rotor Motion Dedicated to the Investigation of the Time-Varying Features of Claw Pole Topologies. *IEEE Trans. Magn.* **2015**, *51*, 211–223. [CrossRef]

23.   Rebhi, R.; Ibala, A.; Masmoudi, A. MEC-Based Sizing of a Hybrid-Excited Claw Pole Generator. *IEEE Trans. Indu. Appl.* **2015**, *51*, 211–223. [CrossRef]

24.   Asfirane, S.; Hlioui, S.; Amara, Y.; Gabsi, M. Study of a Hybrid Excitation Synchronous Machine: Modeling and Experimental Validation. *Math. Comput. Appl.* **2019**, *24*, 34. [CrossRef]